Simulations of nonlinear waves generated by an Air-Cushion Vehicle

Kaiyuan Shi, Renchuan Zhu*, Mengxiao Gu, Xiaocong Wang

State Key Laboratory of Ocean Engineering, School of Naval Architecture, Ocean and Civil Engineering, Shanghai Jiao Tong University, Shanghai 200240, China

Abstract: One major area of interest in air-cushion vehicle (ACV) hydrodynamics is ACV-generated waves. However, the nonlinear effects of varying cushion pressures on the wake system remain unclear. This study presents a fast time-domain method that simulates nonlinear waves. The paper uses a pressure distribution to represent the ACV, models the nonlinear waves by the high-order spectral method, and saves computational effort with damping and domain reconstruction techniques. We simulate the nonlinear waves generated by a constant-speed/accelerating ACV in calm water and by ACV in regular waves, and compare our time-domain results with experimental, CFD, and perturbation theoretical ones. The results show that the nonlinear effects are more pronounced in shallow water and low-speed cases. In the constant-speed case, the maximum wave drag predicted by the nonlinear method is lower than the linear prediction; in the accelerating case, the nonlinear method shows a slight decrease in the Froude number when the resistance reaches the maximum during acceleration. For ACV in waves, nonlinear simulations show a second-order wave component resulting from the interaction between the air cushion and incident waves. This component has little effect on wave force but does contribute to the near-field wave pattern.

Keywords: air-cushion vehicle, nonlinear free-surface flow, wave resistance

1. Introduction

An air-cushion vehicle (ACV), also known as a hovercraft, floats above the surface with the help of high-pressure air below the hull, significantly decreasing drag and enabling high-speed navigation. Unlike traditional marine crafts, there is virtually no contact between the hull and the surface of the water. Therefore, frictional resistance is minimal, and wave-making drag dominates total resistance (Doctors, 1993). In numerical studies, the wave drag of an ACV is calculated from wave elevation. Hence, an accurate simulation and a thorough discussion of ACV-generated waves can help us obtain a better understanding of wave-generation and wave-resistance problems.

Studies of ACV wakes evolved from the general study of ship wakes. Early studies were based on linearized theory, regarding the hovercraft as a pressure disturbance, supposing that wave elevation is linearly proportional to cushion pressure (Doctors, 1993). Lord Kelvin first

Nomenclature

α, β	cushion smooth parameters	F_d	depth Froude number, $F_d=U/\sqrt{gd}$
γ, κ	filter parameters	g	gravitational acceleration
ζ	wave elevation	$\boldsymbol{k}$	wavenumber vector, $\boldsymbol{k} \equiv (k_x, k_y)$
Λ	low-pass filter function	L	ACV length
μ	damping coefficient	l_x, l_y	length of the damping zone
ρ	fluid density of water	L_x, L_y	length of the fluid domain
ϕ	velocity potential	N_x,N_y	grid resolution
ϕ^s	surface velocity potential	p_{ACV}	cushion pressure
B	ACV beam	p_0	average cushion pressure
C_R	resistance coefficient	U	ACV velocity
C_T	transmission coefficient	$\dot{U}$	ACV acceleration
C_w	wave excitation coefficient	$\boldsymbol{x}$	position vector, $\boldsymbol{x} \equiv (x, y)$
d	water depth	x_c, y_c	ACV center position
F_n	Froude number, $F_n=U/\sqrt{gL}$	$\nabla_{\boldsymbol{x}}$	horizontal gradient, $\nabla_{\boldsymbol{x}} \equiv (\partial/\partial x, \partial/\partial y)$

Superscripts

D	disturbance waves	W	wake system
I	incident waves	~	dimensionless variable
E	entire flow field		

Subscripts

t	time derivative, $\partial/\partial t$	z	vertical derivative, $\partial/\partial z$
x	longitudinal derivative, $\partial/\partial x$		

studied the wake generated by a point pressure source and derived the well-known Kelvin wake pattern (Lord Kelvin, 1887). Havelock (1914, 1932) and Lunde (1951) developed equations for the wave resistance of a steadily moving pressure distribution. Newman and Poole (1962) and Barratt (1965) considered an ACV as a uniform rectangular pressure distribution and investigated wave resistance numerically. The wave resistance obtained with this approach agrees well with experiments at high Froude numbers while showing unrealistic oscillations at low Froude numbers. To eliminate these oscillations, Doctors and Sharma (1972) found it necessary to apply a smoothing function to the edges of the pressure distribution. A simplified formula for steady wave resistance, which filters the local flow component, also shows good agreement with Doctors' approach (Noblesse *et al*., 2009, 2011). In recent years, several studies have been conducted on wakes generated from ACVs sailing in ice fields (Li *et al*., 2017; Sturova *et al*., 2019; Xue *et al*., 2021). Regarding wakes in unsteady motion, Doctors *et al*. (1972, 1975, 1980) investigated wave drag during acceleration using a method based on the Laplace transform in the time domain. Yeung (1975) proposed an approach to predict waves generated by an ACV under arbitrary motion with the help of the associated kernel function.

The studies mentioned above, which are based on linearized theory, neglect the nonlinear effects of cushion pressure and may overestimate wave resistance in shallow water (Doctors, 1993). Much effort has been focused on simulating nonlinear ACV wakes and wave drag.

Doctors and Dagan (1980) compared wave resistance calculated using different methods for a steadily moving two-dimensional pressure distribution. The results show that the secondary and tertiary perturbation solutions agree well with the fully nonlinear numerical results proposed by Kerczek (1977). Another innovative method solves the two-dimensional case in the complex-wavenumber plane, which can achieve convergence across several iterations (Schwartz, 1981). Sung and Grilli (2008) presented a three-dimensional boundary element method to solve the steady flow problem. This method takes linearithmic time because of the use of the fast multipole algorithm. Nikseresht *et al*. (2008) solved the Navier–Stokes equations using the finite volume method and predicted the resistance of a constant-speed ACV. Bhushan *et al*. (2011, 2017) studied wave drag for straight-ahead and yawed ACVs with an unsteady Reynolds-averaged Navier–Stokes (URANS) model and found that nonlinearity may contribute to wave drag in shallow water and the low-intermediate Froude number case. Maki *et al*. (2012, 2013) compared the wave drag of the pressure distribution with the linear method and URANS, with results suggesting that fluid viscosity is almost irrelevant to wave drag.

The study of nonlinear ACV wakes may be inspired by the more general field of studies of ship wakes. Dommermuth and Yue (1988) investigated nonlinear steady-state ship wakes created by a pressure disturbance with the high-order spectral (HOS) method. Dam *et al*. (2006, 2008) studied the propagation of ship waves in different seabed topographies. Using the Boussinesq-type wave model with a pressure term, the solitary waves ahead of the ship (Torsvik and Soomere, 2008; Torsvik *et al*., 2015; Shi and Malej, 2017) and the far-field interaction of ship waves (David *et al*., 2017) have been studied. Pethiyagoda *et al*. (2017, 2018) conducted intensive studies on the spectrum of wave elevation at the probe as well as the transverse waves at low Froude numbers. Grue (2017) reported large waves created by a ship passing through an abrupt depth transition and reproduced the phenomenon numerically using a pressure disturbance. A series of very recent papers approximate the ship as a pressure field and investigated the apparent angle of ship waves (Colen *et al.*, 2021; Pethiyagoda1 e*t al.*, 2021; Lo, 2021).

Previous studies of nonlinear waves generated by an ACV have been limited to steadily moving cases in calm water (Maki *et al*., 2012, 2013; Bhushan *et al*., 2011, 2017). The nonlinear effects of cushion pressure on ACV wakes and wave drags under unsteady conditions remain unclear. This paper introduces an efficient time-domain method to simulate nonlinear ACV wakes. The HOS method is extended to model the waves created by a moving pressure distribution, which denotes the ACV. The computational domain is reconstructed at each time step to ensure that the ship is centered so that arbitrary ship motions can be simulated using limited computational resources. Using the proposed method, we studied nonlinear waves generated by the ACV at varying cushion pressures.

This study provides the investigation into the nonlinear effects of cushion pressure on

waves generated by accelerating ACV in calm water and constant-speed ACV in regular waves. We found that the Froude number that corresponds to the maximum wave drag during acceleration is slightly less than the linear prediction when nonlinearity is taken into account, and this may help evaluate ACV resistance more accurately. Moreover, the study reveals the nonlinear wave component that resulted from the interaction between the incident wave system and the ACV wake system, which we termed the transmission component. The wave amplitude of the transmission component varies periodically and may reach up to 7–20% of the incident wave amplitude; thus, it may affect the motion response in waves.

2. Numerical methods

2.1 Problem setup

The contact between skirt and water is commonly neglected in the study of waves generated by a hovercraft, and therefore the ACV may be equivalent to the pressure distribution (Doctors *et al*., 1993). We consider the fluid to be incompressible and inviscid and the flow to be irrotational. The flow field can be described using potential flow theories. A 3D Cartesian coordinate system is adopted with its origin located at the mean water level and the z-axis pointing vertically upwards. In the Eulerian specification, the governing equation and boundary conditions are written as follows:

$$\begin{cases} \nabla^2\phi = 0 & \\ \zeta_t + \nabla_x\phi\cdot\nabla_x\zeta - \phi_z = 0 & on\ \ z=\zeta \\ \phi_t + \frac{1}{2}(\nabla\phi)^2 + g\zeta = \frac{p_{ACV}}{\rho} & on\ \ z=\zeta \\ \phi_z = 0 & on\ \ z=-d \end{cases} \tag{1}$$

where $\phi(\boldsymbol{x}, z, t)$ is the velocity potential, $\zeta(\boldsymbol{x}, t)$ is the wave elevation, d is the water depth, g is the gravitational acceleration, and ρ is the fluid density. $\boldsymbol{x} \equiv (x, y)$ is the vector in the horizontal plane; the subscripts t, z denotes the partial derivative of t, z respectively; and $\nabla_x \equiv (\partial/\partial x, \partial/\partial y)$ denotes the horizontal gradient.

In Eq. (1), the flow field is described in an earth-fixed coordinate system, and p_{ACV} represents a maneuvering ACV with arbitrary motion. Following Doctors and Sharma (1972), the ACV studied in this paper is modeled as a rectangular smooth edged pressure distribution of length L, beam B:

$$\begin{aligned} p_{ACV} = \frac{p_0}{4} &\times \left\{ \tanh\left[\alpha\left(\frac{x-x_c}{L}+\frac{1}{2}\right)\right] - \tanh\left[\alpha\left(\frac{x-x_c}{L}-\frac{1}{2}\right)\right]\right\} \\ &\times \left\{ \tanh\left[\beta\left(\frac{y-y_c}{B}+\frac{1}{2}\right)\right] - \tanh\left[\beta\left(\frac{y-y_c}{B}-\frac{1}{2}\right)\right]\right\} \end{aligned} \tag{2}$$

where p_0 is the average cushion pressure, and (x_c, y_c) is the ACV center position. α, β are

smoothing factors. Unless otherwise stated, in this paper, *L/B* defaults to 3/2 and α, β are 24. As the ACV moves, p_{ACV} (expressed in the earth-fixed coordinate system) changes over time. The time-domain method proposed in this paper enables simulations not only of constant pressure distributions but also of temporally varying distributions. More realistic results can be obtained with a cushion model that involves fan and air leakage.

2.2 HOS method with moving pressure distribution

Over the past decades, many efficient numerical methods have been developed to deal with nonlinear free-surface conditions, such as the HOS method based on the Taylor expansions (Dommermuth and Yue, 1987, 1988; West *et al*., 1987, Xiao *et al*., 2019), Boussinesq-type wave models with generalized minimum residual method solver (Boussinesq, 1872; Madsen *et al*., 2002; Fuhrman *et al*., 2004; James *et al*., 2006), the spectral boundary integral (SBI) method, based on the Green function (Clamond *et al*., 2001, 2005; Fructus *et al*., 2005, 2007). Among these, the HOS method might be the quickest but may not converge for cases with extremely steep waves. Fortunately, the depth-length ratio of ACV is much smaller than that of a conventional ship, which results in a relatively gentle wave steepness (Bhushan *et al*., 2017) and fits the HOS simulation. For extremely high cushion pressure or changing seabed topography, the SBI or Boussinesq approaches may be applied as well.

As proposed by Zakharov (1968), the surface potential could be defined as follows:

$$\phi^s(\boldsymbol{x},t) = \phi(\boldsymbol{x},\zeta(\boldsymbol{x},t),t) \tag{3}$$

The chain rule allows us to deduce the kinematic and dynamic boundary conditions:

$$\begin{aligned} \zeta_t &= (1+(\nabla_x\zeta)^2)\phi_z - \nabla_x\phi^s\cdot\nabla_x\zeta \qquad on\ \ z=\zeta \\ \phi_t^s &= -\frac{1}{2}(\nabla\phi^s)^2 + \frac{1}{2}(1+(\nabla_x\zeta)^2)\phi_z^2 - g\zeta - \frac{p_{ACV}}{\rho} \quad on\ \ z=\zeta \end{aligned} \tag{4}$$

For the initial conditions, $\phi^s(\mathbf{x},0)$ and $\zeta(\mathbf{x}, 0)$ are given. In Eq. (4), horizontal derivatives can be directly calculated by differential or spectral methods. The HOS method is adopted to obtain ϕ_z. Here we give a brief introduction to the method. More details can be found in Dommermuth and Yue (1987).

First, we expand ϕ in a perturbation series:

$$\phi = \phi^{(0)} + \phi^{(1)} + \phi^{(2)} + \cdots \tag{5}$$

Then, the Taylor expansion is carried out on ϕ at $z = 0$, we have:

$$\begin{aligned} \phi^s = \phi(\mathbf{x},\zeta,t) &= \phi^{(0)}(\mathbf{x},0,t) + \zeta\phi_z^{(0)}(\mathbf{x},0,t) + \frac{\zeta^2}{2}\phi_{zz}^{(0)}(\mathbf{x},0,t) + \cdots \\ &+ \phi^{(1)}(\mathbf{x},0,t) + \zeta\phi_z^{(1)}(\mathbf{x},0,t) + \cdots \\ &+ \phi^{(2)}(\mathbf{x},0,t) + \cdots \\ &+ \ldots. \end{aligned} \tag{6}$$

Thus, we can obtain a series of boundary conditions at $z = 0$:

$$\begin{aligned} \phi^{(0)}(\mathbf{x},0,t) &= \phi^{s} \\ \phi^{(m)}(\mathbf{x},0,t) &= -\sum_{k=1}^{m}\frac{\zeta^{k}}{k!}\frac{\partial^{k}}{\partial z^{k}}(\phi^{(m-k)}(\mathbf{x},0,t)) \ , \quad m \geq 1 \end{aligned} \tag{7}$$

ϕ_z can be calculated by the following equation:

$$\phi_z(\mathbf{x},\zeta,t) = \sum_{k=1}^{M}\left(\frac{\zeta^{k-1}}{(k-1)!}\frac{\partial^{k}}{\partial z^{k}}\left(\sum_{m=1}^{M-k+1}\phi^{(m)}\right)\right) \tag{8}$$

Here M is the HOS truncation order. In the numerical implementation, ϕ^s and ζ are assumed to satisfy the periodic boundary condition and discretized into sets of uniformly spaced grids, therefore fast Fourier transform (FFT) can be used to calculate the derivative of $\phi^{(m)}$ with eigenfunction expansions represented in the following forms:

$$\begin{aligned} \phi^{(m)}(\boldsymbol{x},z,t) &= \sum A(t)e^{|\boldsymbol{k}|z}e^{i\boldsymbol{k}\boldsymbol{x}} && \textit{for infinite water depth} \\ \phi^{(m)}(\boldsymbol{x},z,t) &= \sum A(t)\frac{\cosh(|\boldsymbol{k}|(z+d))}{\sinh(|\boldsymbol{k}|d)}e^{i\boldsymbol{k}\boldsymbol{x}} && \textit{for finite water depth } d \end{aligned} \tag{9}$$

where $\boldsymbol{k} \equiv (k_x, k_y)$ is the wavenumber vector.

In this study, the fourth-order explicit Runge–Kutta scheme is used to integrate Eq. (4). For numerical stability and de-aliasing, all FFT operations are performed with a low-pass filter in the wavenumber space. As proposed by Xiao *et al*. (2013), the filter takes the form:

$$\Lambda(\boldsymbol{k}) = \exp\left(-\left|\frac{\gamma|\boldsymbol{k}|}{|\boldsymbol{k}_{max}|}\right|^{\kappa}\right) \tag{10}$$

where $\boldsymbol{k}_{max}$ is the maximum wavenumber and $\gamma = 2.2$, $\kappa = 30$ are filter parameters.

2.3 Attention mechanism

As described in Section 2.1, this paper studies ship wakes in an earth-fixed reference frame. That is, in the numerical implementation, the horizontal coordinates of each grid remain invariant. The benefit of this practice is that it eliminates all of the troubles associated with mesh movement. However, as the ship continues to move away from its initial position, a large computational domain is required to cover the range of ship motion and wave propagation. Once the ACV reaches a boundary, the simulation cannot continue. To save computational resources while allowing for arbitrary ship motion, we use a special domain reconstruction and damping technique, which we call the attention mechanism.

The attention mechanism works somewhat like a camera with a limited field of view that keeps track of the ship's position and does not take images away from the ship. The position of

the ACV is checked at each timestep. Once the ACV escapes the pre-defined area, a reconstruction is triggered to reset the computational domain. As discussed in Section 2.2, a set of uniformly spaced grids is used to model the fluid domain. In the reconstruction process, the grid points at the domain boundary that are moving away from the ACV are removed, some points closer to ACV are newly added, and most of the grid points remain unchanged, as presented in Fig. 1. During this process, the number of grid points remains unchanged, and the memory freed up by the deletion of grid points is used to store information about the newly added points.

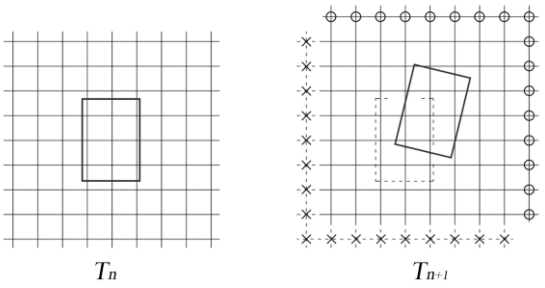

Fig. 1. Domain reconstruction (×, deleted grid points; ○, newly added grid points).

To define the data source for the newly added grid points, we divide the entire flow field into two parts: incident wave components and disturbance wave components. The wave elevation and velocity potential for the added points are derived from the incident wave component. The far-field disturbance components will propagate outwards and have little effect on the calculation of near-field components. A damping strategy is applied near to the boundary to absorb the disturbance component, so only the incident wave components are left at the boundary, and point addition/deletion does not induce abrupt changes to the flow field.

We use subscripts *E*, *I*, and *D* to denote the entire flow field, incident waves, and disturbance waves, respectively. Wave elevation ζ^E and velocity potential ϕ^E, which include both incident wave and disturbance components, are calculated through the integration of Eq. (4), allowing the simulation of various nonlinear interactions. ζ^I and ϕ^I, which represent the incident wave, can be obtained from stokes wave theory or from HOS simulation. In this paper, we use another HOS simulation to obtain the incident wave flow field. The incident wave simulation satisfies the periodic boundary conditions and shares the same initial conditions, time steps and grid parameters as the entire flow field simulation but does not contain the pressure term. When the entire flow field and the incident flow field are known, the disturbance flow field can be separated out as follows:

$$\begin{aligned} \zeta^D &= \zeta^E - \zeta^I \\ \phi^D &= \phi^E - \phi^I \end{aligned} \tag{11}$$

To achieve the damping of far-field disturbance waves, artificial viscosity terms are

introduced to Eq. (4):

$$\begin{aligned} \zeta_t^E &= (1+(\nabla_{\mathbf{x}}\zeta^E)^2)\phi_z^E - \nabla_{\mathbf{x}}\phi^E \cdot \nabla_{\mathbf{x}}\zeta^E - \mu\zeta^D \quad on\ \ z=\zeta^E \\ \phi_t^E &= -\frac{1}{2}(\nabla\phi^E)^2 + \frac{1}{2}(1+(\nabla_{\mathbf{x}}\zeta^E)^2)\left(\phi_z^E\right)^2 - g\zeta^E - \frac{p_{ACV}}{\rho} - \mu\phi^D \quad on\ \ z=\zeta^E \end{aligned} \tag{12}$$

where μ takes the non-zero value only on the margin of the computational domain

$$\mu(x,y) = \mu_0\left(1-\sin\left(\frac{\pi}{2}s_x\right)^{0.1}\right)\left(1-\sin\left(\frac{\pi}{2}s_y\right)^{0.1}\right) \tag{13}$$

$$\begin{aligned} s_x &= \begin{cases} d_x / l_x & for\ \ d_x < l_x \\ 1 & for\ \ d_x \geq l_x \end{cases} \\ s_y &= \begin{cases} d_y / l_y & for\ \ d_y < l_y \\ 1 & for\ \ d_y \geq l_y \end{cases} \end{aligned} \tag{14}$$

where d_x, d_y are the minimum distances between a field point and the boundaries, and l_x, l_y are the lengths of the damping zone.

2.4 Wave force calculation

According to Newton's third law, the force exerted by the wave on the air cushion is equal in magnitude to the force exerted by the pressure distribution on the wave. As shown in Fig. 2, the force of the pressure along the *x*-axis on the free surface is calculated with the *x*-directional derivative of the wave elevation, and the wave force can be obtained by integration, as in Eq. (15).

$$F = -\iint p_{ACV}\zeta_x dxdy \tag{15}$$

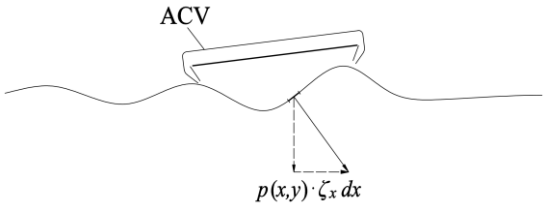

Fig. 2. The force exerted by pressure distribution on the wave.

In the absence of incident wave excitation, ζ_x is independent of the average cushion pressure p_0. We use the superscript W to denote the contribution of the ship wake. Then, when the ship is sailing in calm water, the drag coefficient can be defined as follows:

$$C_R = -\frac{\rho g}{p_0^2 B}\iint p_{ACV}\zeta_x^W dxdy \tag{16}$$

When wave excitation is present, in addition to the contribution of the wake system, there

is a periodically varying component. The dominant part of this periodic component is the incident wave, whose ζ_x is independent of the mean pressure and is related to the wave steepness *kA*. Therefore, one can define the excitation coefficient as:

$$C_w = \frac{1}{kA}\frac{\rho g}{p_0 B}\iint p_{ACV}\zeta_x dxdy \tag{17}$$

where ζ_x is a periodically varying variable that can be substituted for either the incident wave, the nonlinear interaction of the incident wave and the ship wake, or the sum of the two. Since the excitation varies periodically with time, we only take the magnitude for comparison. Among them, the nonlinear interaction is of special concern and we name it as the transmission coefficient C_T, identified by subtracting the entire flow field from the incident wave and ship wake.

$$C_T = \frac{1}{kA}\frac{\rho g}{p_0^2 B}\iint p_{ACV}\left(\zeta_x^E - \zeta_x^I - \zeta_x^W\right)dxdy \tag{18}$$

A flow chart illustrating the procedure of the numerical implementation is presented in Fig. 3.

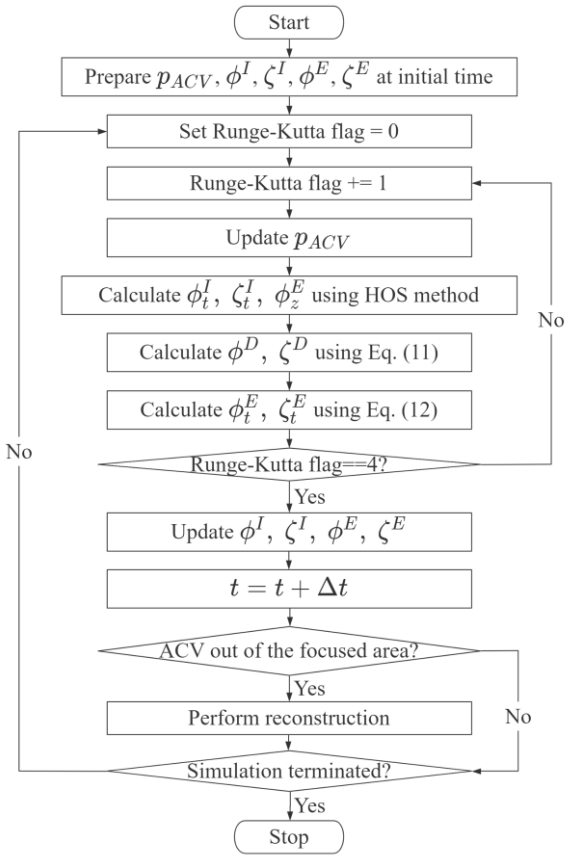

Fig. 3. Flow chart of the present method.

Following the numerical approach mentioned above, we developed a Python program to simulate nonlinear wave elevation. Matrix operations and FFT/IFFT are implemented by the

PyTorch library and can be parallelized using either the CPU backend or the GPU backend. A significant acceleration could be achieved using the GPU backend, as illustrated in Fig. 4. The simulations are performed on a personal computer with an AMD 3700X CPU and an NVIDIA RTX2060 graphics card. For a 512 × 512 grid, it takes 0.17 s per timestep with 8-core message passing interface parallelism, compared to 0.02 s with a GPU backend.

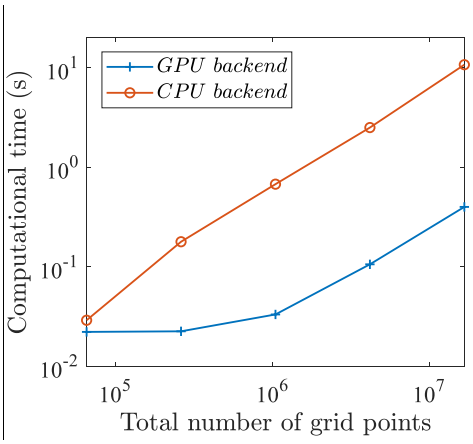

Fig. 4. Computation time per timestep with different backends.

3. Results and discussion

3.1 Model setup and convergence analyses

Convergence tests are first conducted to ensure that the appropriate grid resolution and domain size are adopted in the simulations. At small Froude numbers, the wavelength of the ship wake can be very short, so a coarse grid may not be sufficient to model the wake. Larger Froude numbers correspond to longer wavelengths, which makes it difficult for disturbance waves to be absorbed in a small computational domain. Therefore, the wave force only achieves convergence when the grid is sufficiently fine and the domain is large enough. We prepared five sets of grids with different domain sizes and grid resolutions, as shown in Table 1. L_x, L_y denote the domain size and l_x, l_y denote the damping length, as shown in Fig. 5. N_x, N_y are the number of grids along the x-axis and y-axis, respectively. In Table 1, Grids 1–3 have the same domain size and damping length but of different grid resolutions, while Grids 2, 4, and 5 are of the same grid resolutions but different domain sizes.

Table 1. Size of the computational domain and grid resolution.

Grid No.	L_x	L_y	l_x	l_y	N_x	N_x
Grid 1	16L	16L	4L	4L	256	256
Grid 2	16L	16L	4L	4L	512	512
Grid 3	16L	16L	4L	4L	1024	1024
Grid 4	8L	8L	2L	2L	256	256
Grid 5	32L	32L	8L	8L	1024	1024

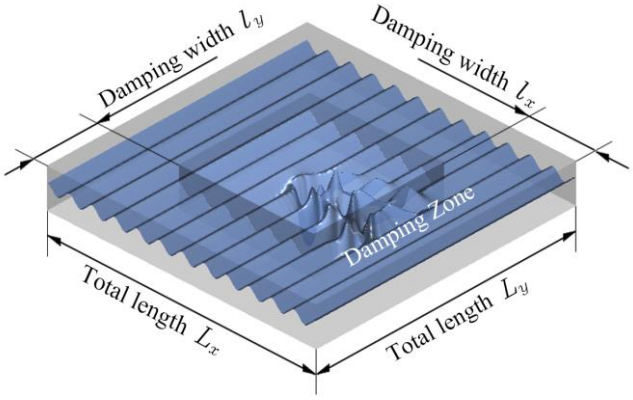

Fig. 5. Dimensional parameters of the domain.

Fig. 6 plots the wave resistance of a constant-speed ACV in infinite water depth. As shown in Fig. 6(a), wave drag calculated with Grids 2 and 3 are identical, while Grid 1 shows inconsistencies with the other two sets of grids at low Froude numbers. In Fig. 6(b), the results for Grids 2 and 5 are in good agreement, and Grid 4 deviates from the results of Grids 2 and 5 at high Froude numbers due to inadequate damping. In the figure, we consider that Grid 2 is fine enough to capture change in wave elevation and large enough to absorb far-field waves without affecting the near-field components. Unless otherwise stated, simulations in the latter part of the paper are carried out on Grid 2.

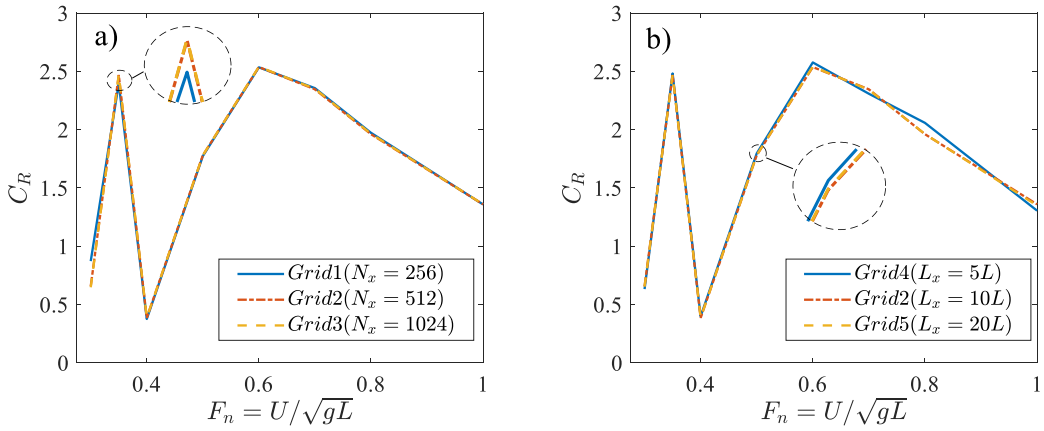

Fig. 6. Wave resistance convergence: (a) grids with different grid spacing, (b) grids with different domain sizes.

The HOS order M is an important parameter related to computational efficiency and accuracy. An increase in M will exponentially reduce the truncation error of the nonlinear calculation, however, the computation effort will increase as well. In this paper, The discussions on domain size, grid resolution, and computational efficiency are based on M = 3. And it is verified that all numerical results shown in this paper converge at $M \geq 3$ with errors within 2%.

Among the figures shown hereafter, the case with the greatest wave steepness is an ACV traveling in shallow water at F_n=0.4. The wave profiles calculated with different orders M are

plotted in Fig. 7, where the two curves for $M \geq 3$ overlap, indicating that $M = 3$ is adequate for accuracy.

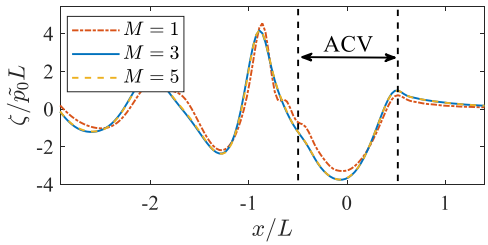

Fig. 7. Longitudinal slice of the wave elevation calculated by M = 1,3,5 ($\tilde{p}_0$ = 0.0127, F_n=0.4, d/L=0.215)

3.2 Waves generated by a constant-speed ACV

To obtain the steady wave drag, the ACV accelerates uniformly from rest and then turns to move at a constant speed after reaching the required velocity. The wave drag coefficient is evaluated from the average value of the time history after the steady state. The dimensionless parameter $\tilde{p}_0 = p_0 / \rho g L$ is defined to characterize the average pressure of the hovercraft. Figs. 8 illustrate the wave resistance coefficient at various pressure levels, and our time-domain results are compared to linear theory (see Appendix A.2), experiment (Everest, 1966; Everest and Hogben, 1967), and CFD predictions (Bhushan *et al.*, 2011).

The resistance curves in Fig. 8 fluctuate with the Froude number, presenting *humps and hollows*, which was perhaps first described by Newman and Poole (1962). Wave drags obtained by different methods show the same tendency, with humps and hollows close in position and magnitude. In both deep and shallow water, the results at low pressure level ($\tilde{p}_0 = 0.0001$) are almost exactly consistent with the linear solution, and CFD simulations are in good agreement with the nonlinear potential flow predictions ($\tilde{p}_0 = 0.0127$), which demonstrates the validity of the proposed method.

The experimental data are taken from the study conducted by Everest and Hogben (1967). In their work the deep water resistance is calculated from the wave pattern, while the shallow water resistance is estimated from the trim attitude and may contain other drag components. The experiment results in Fig. 8(a) are roughly consistent with the numerical simulation, but around resistance hump there exist some scatter points, with larger resistance than that of the numerical predictions. The difference may be mainly due to the fact that the experiment cannot obtain *pure wave drag* without involving the disturbance of spray, cushion pressure pulsation, and other interference factors. Another major cause of the discrepancy is that the numerical simulation assumes that the cushion pressure is a distribution with smooth edges that does not vary with time, which differs from the actual cushion. Since the experimental data in Fig. 8(b)

are derived from the trim angle, it will be impacted by a larger variety of sources (e.g. towing mechanism), and exhibit greater differences (Doctors, 1993).

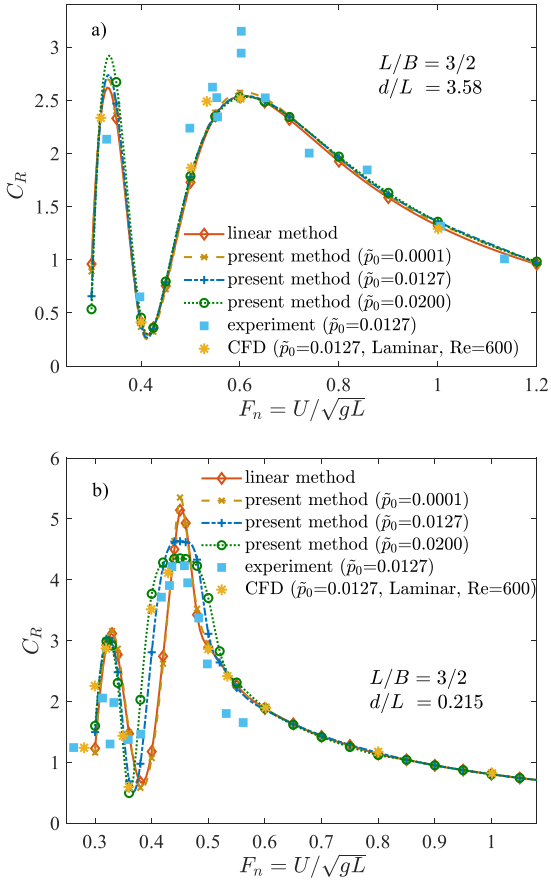

Fig. 8. Wave resistance coefficient for the ACV in in (a) deep water (b) shallow water.

For a hovercraft traveling at constant speed in deep water, Fig. 8(a) demonstrates that the nonlinearity brought about by increasing the pressure level has virtually no effect on the wave drag. Wave drags obtained by the time-domain method at different pressure levels are almost identical to the linear prediction. However, the consistency in wave resistance does not mean that the wave elevation is also the same. For instance, in Fig. 9, higher cushion pressures lead to shorter wavelengths in the wake and cause a bulging wave to appear behind the ship.

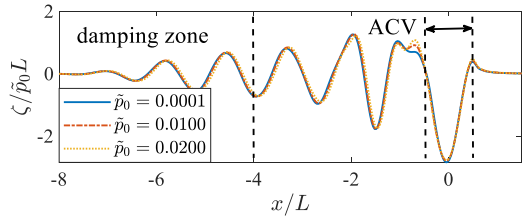

Fig. 9. Longitudinal slice of the wave elevation at different pressure levels in deep water (F_n=0.45, d/L=3.58)

In shallow water, the curves in Fig. 8(b) exhibit the tendency of a leftward shift of the resistance hollow as the cushion pressure increases, as well as a decrease of the maximum resistance. Such phenomena can also be found in CFD and experimental results. Due to the

nonlinearity, drag in the range F_n = 0.32–0.36 will drop at a greater slope and enter the rising zone a little earlier after passing through the hollow. In shallow water case, F_n = 0.46 is the critical speed, where the depth Froude number F_d=$U/\sqrt{gd}$ =1. Here the craft speed is close to the maximum wave velocity in shallow water, and drag is at its maximum. It should be noted that the ship will keep creating huge solitary waves ahead when traveling around the critical speed (Li and Sclavounos, 2002), which cannot be captured within the framework of linear theory. Since the hydrodynamics of solitary waves is subject to the tank width, the wave drag obtained from experiments and CFD may not be exactly the resistance in an unbounded domain. With high cushion pressure, Grid2 is not large enough to model the solitary wave, and Grid5 is adopted to bring the wave drag to convergence. Through nonlinear time-domain simulations, it turns out that the increase in cushion pressure will widen the velocity interval in which the solitary wave could appear. This phenomenon may account for the broadening of the resistance hump in Figure 8(b).

For further study, we graphed the near-field wave elevation around F_n = 0.45. The longitudinal/transversal slices at the center of the ACV are plotted in Fig. 10. Despite the equal spacing of the pressures, the differences in wave elevation are not equal, which suggests the presence of nonlinear components that are higher than the second order. Compared to the longitudinal slices for $\tilde{p}_0 = 0.0001$, the wave profiles are elevated fore and aft for $\tilde{p}_0 = 0.0064, 0.0127$. With the waves rising at both ends, the effects of nonlinearity on drag are canceled out and are not as great as the effect on wave elevation.

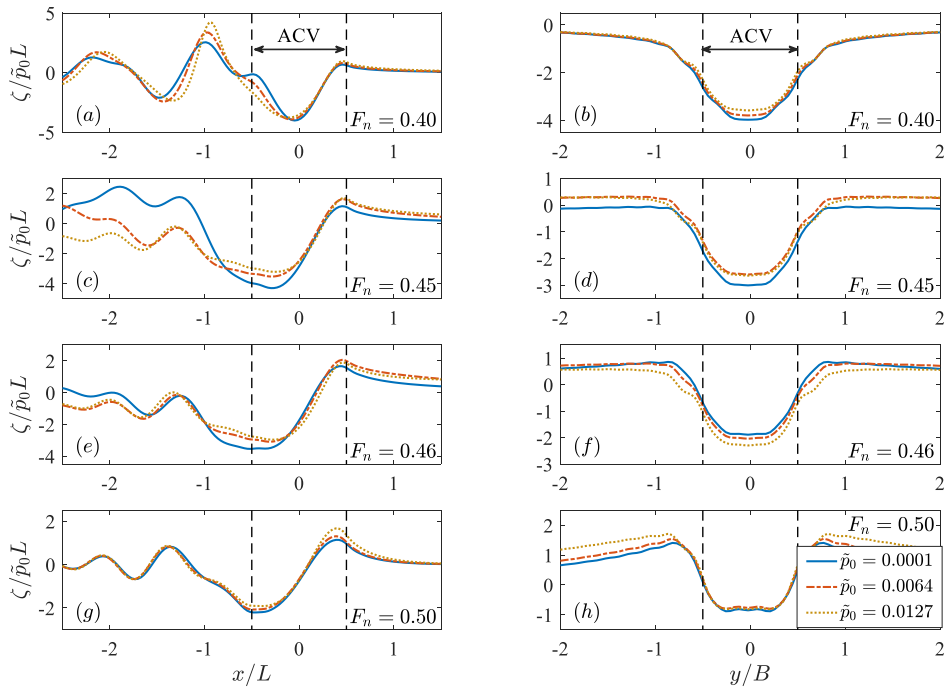

Fig. 10. Longitudinal/transversal slices of the wave elevation in shallow water (d/L = 0.215).

Fig. 11 shows the wave pattern for an ACV in shallow water around F_n = 0.45. As can be seen in Figs. 10 and 11, the wave troughs become flatter, and the wave crests become steeper

in higher-pressure cases, which is typical for nonlinear shallow-water waves. Figs. 11(a) shows that higher pressure corresponds to shorter wavelengths when $F_d < 1$. This might be because higher amplitudes result in a greater velocity for a wave of the same wavelength. In higher-pressure cases, shorter wavelengths are required to keep the wave system moving with the ship. This may also account for the leftward shift of the resistance curve in Fig. 8(b). Fig. 11(d) gives the wave pattern for $F_d > 1$, and a larger wave crest is observed in front of the ACV for $\tilde{p}_0 = 0.0127$, causing resistance coefficients to be greater than the linear case.

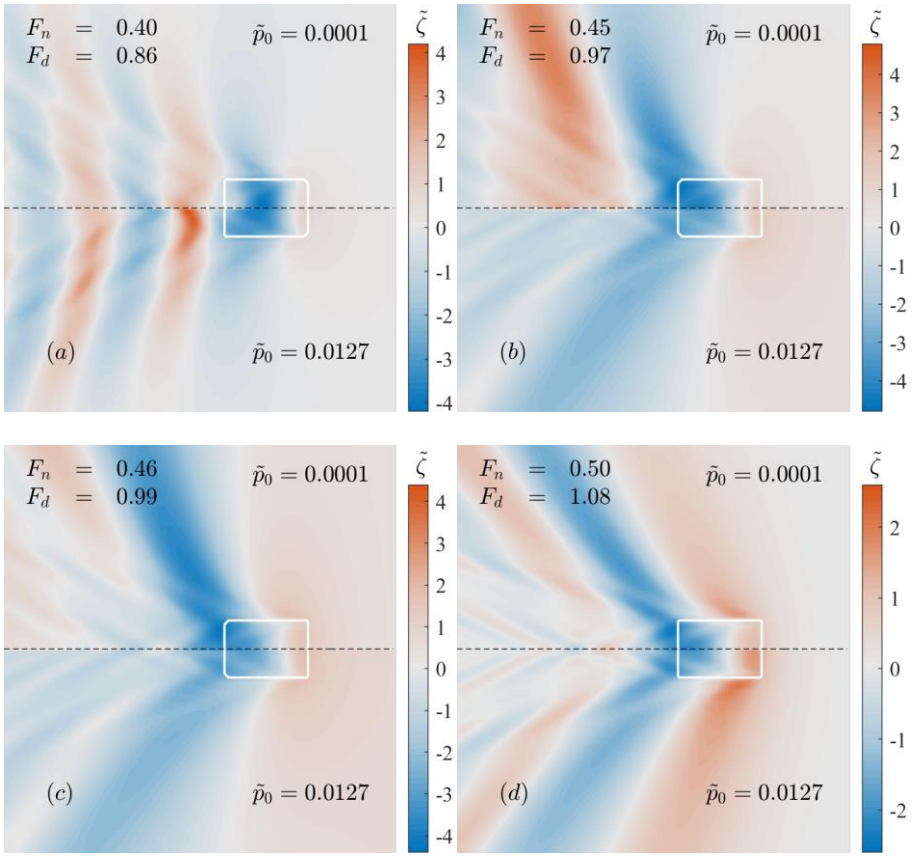

Fig. 11. Wave patterns for a steady-moving hovercraft in shallow water (d/L = 0.215).

3.3 Waves generated by an accelerating ACV

The cruising speed of an ACV is far above the hump speed, so maximum drag occurs during acceleration. Previous experimental and theoretical studies have found that peak resistance during acceleration will be greatly reduced in shallow water (Doctors and Sharma, 1972; Doctors, 1975). Consequently, it is valuable to investigate the effects of nonlinearity on accelerating motion.

For validation, the resistance curve of an ACV accelerating from rest with the acceleration $\dot{U} = 0.1g$ is calculated and compared with the linear results by Doctors and Sharma (1972) and Yeung (1975). A very low pressure ($\tilde{p}_0 = 0.0001$) is adopted in the time-domain simulation to

minimize the nonlinear effects. Perfect agreement between the three methods can be seen in Fig. 12. Compared with previous methods, the method proposed in this paper allows the simulation of nonlinear effects, may be simpler to implement, and can fully exploit the performance of modern graphics cards, which shows a promising future.

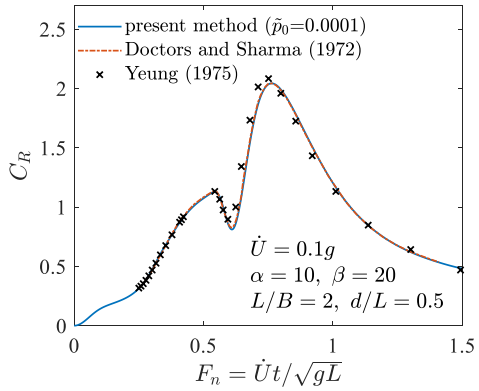

Fig. 12. Wave resistance of an accelerating hovercraft calculated by different methods.

Fig. 13 shows the wave drag of an accelerating ACV at various pressure levels. When the acceleration is small ($\dot{U} = 0.005g$), the resistance curves are quite similar to steady-state curves, with oscillations at low Froude numbers. As the acceleration grows, the oscillations disappear, accompanied by the rightward shift of the humps and hollows in the curve. A significant reduction in resistance is observed in shallow water cases, where a higher cushion pressure may push the location of the humps and hollows to lower speeds. Contrary to the constant-speed cases, the nonlinear effect on the maximum drag is not pronounced in shallow water, which is probably because there is not enough time for the acceleration process to generate solitary waves ahead of the ship. The nonlinearity only slightly decreases the hump speed, and the greater the acceleration, the weaker the nonlinearity.

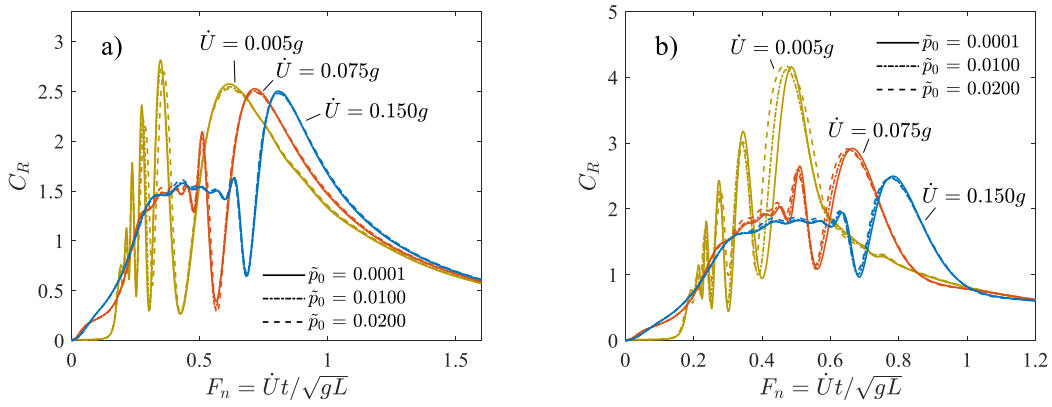

Fig. 13. Wave resistance of hovercraft with uniform acceleration (L/B = 3/2) (a) deep water (d/L = 3.58) (b) shallow water (d/L = 0.215).

Examining the acceleration performance of an ACV, we mainly focus on the location and magnitude of the resistance hump, which determines the maximum power during acceleration.

We graphed the wave patterns at the hump speed in acceleration to investigate the nonlinear effect, as shown in Figs. 14–16. Fig. 14 illustrates that there must be a crest in the fore and a trough in the aft at the moment of maximum resistance. The nonlinear effect is not significant in cases in deep water, as shown in Figs. 14(a) and 15. The wave patterns exhibit more pronounced nonlinear features, with steeper crests, flatter troughs, and shorter wavelengths in Figs. 14(b) and 16.

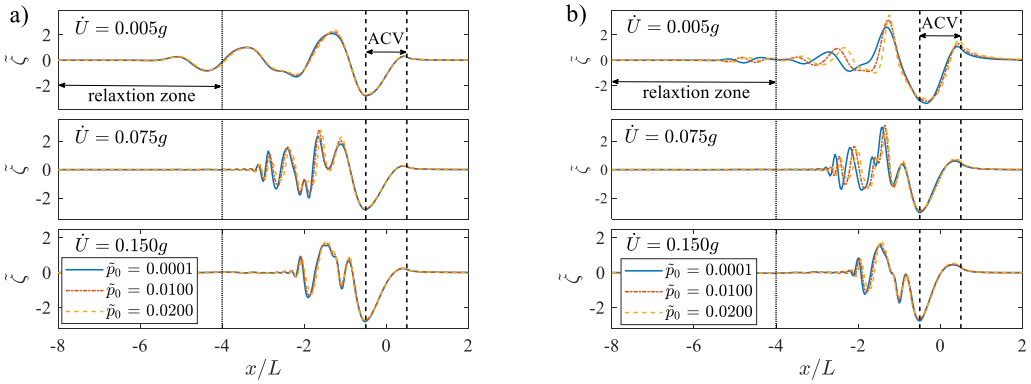

Fig. 14. Longitudinal slices at hump speed (a) d/L = 3.58 (b) d/L = 0.215.

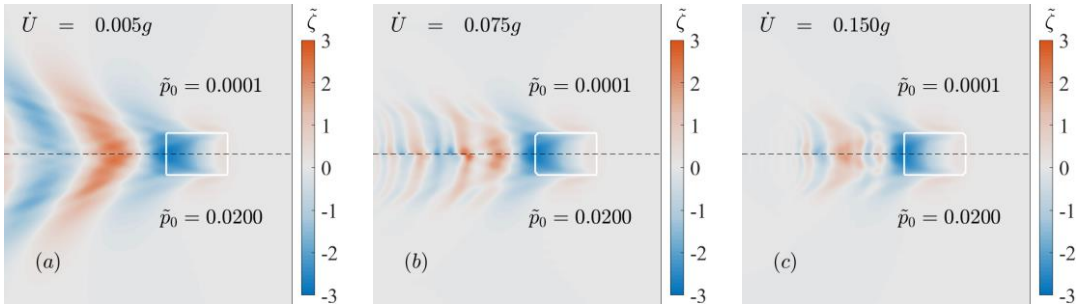

Fig. 15. Wave patterns at the hump speed for uniformly accelerating motion (d/L = 3.58).

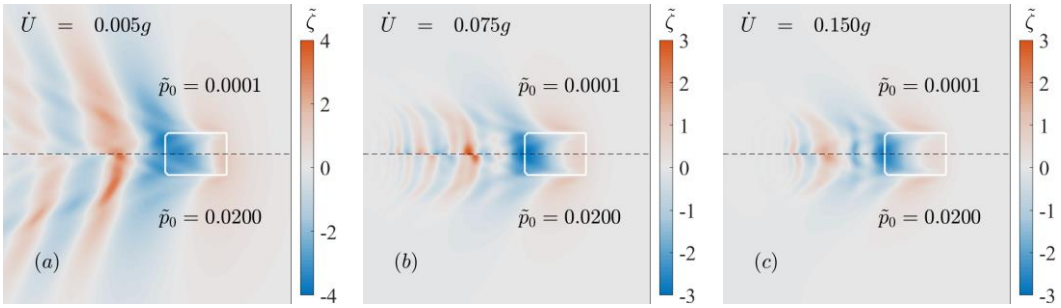

Fig. 16. Wave patterns at the hump speed for uniformly accelerating motion (d/L = 0.215).

3.4 Nonlinear interaction between the incident wave and pressure distribution

The existing literature, when studying the effect of incident waves on an ACV, assumes that the incident waves can pass through the ship wake without hindrance (Guo *et al*., 2018; Gao *et al*., 2021). This assumption allows the incident wave to be independent and simplifies the

problem. But obviously, the interaction between the incident wave and the ACV wake is neglected. This nonlinear interaction, which we call the transmission component in this paper, may manifest itself in two aspects: first, it produces excitation forces, which directly affect the ACV motion response; second, it changes the leakage height of the cushion, which indirectly causes effects on the air cushion dynamics. In this section, the forces and wave patterns caused by the transmitted components are investigated with regular waves as the incident wave excitation.

To ensure that the time-domain method gives proper results, we derived a frequency-domain expression using second-order perturbation theory for comparison. We consider the transmission force to be approximately proportional to the amplitude of the incident wave and cushion pressure. Therefore, a complex expression for the transmission waves is derived from frequency-domain equations (see Appendix A.3). Fig. 17 shows the time history of the transmission coefficient obtained by the two methods. The time-domain transmission coefficient gradually establish a periodic steady-state over time, and the steady-state amplitude and phase agree with the perturbation prediction. The upper half of Fig. 18 is the wave pattern of a randomly selected moment after the time-domain simulation reaches the steady-state, while the lower half is the wave pattern of the same phase according to the perturbation derivation. The wave patterns obtained from the two methods are in good agreement, suggesting that this nonlinear component may be mainly of second order.

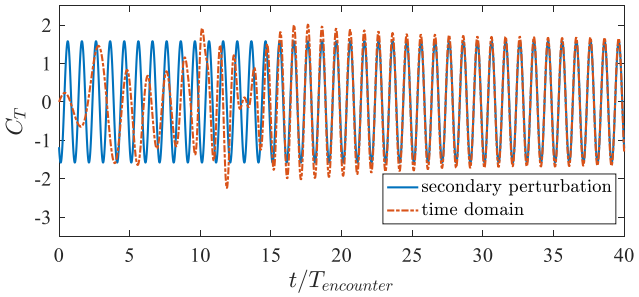

Fig. 17. Time history of the transmission coefficient (F_n = 0.6, λ/L = 0.76, kA = 0.005, d/L = 0.215).

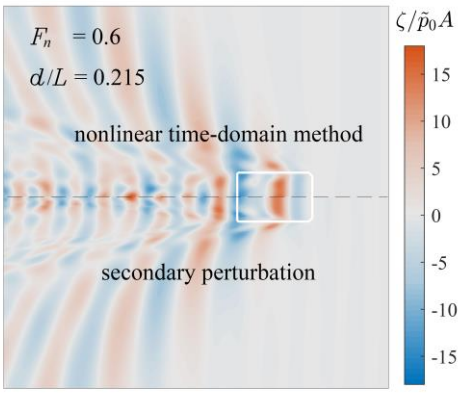

Fig. 18. Wave pattern of the transmission component calculated by different methods.

Figs. 19 and 20 present the wave force coefficients calculated by the perturbation method under different Froude numbers and wavelengths. Because the incident force is approximately proportional to the cushion pressure, and the transmission force is proportional to the square of the cushion pressure, the ratio of the transmission force to incident force is determined by the dimensionless factor $\tilde{p}_0$. Figs. 19 and 20 indicate that the nonlinear interactions are stronger in shallow water than in deep water. These nonlinear effects are more significant in cases with low speeds and short wavelengths. Due to the high cruising speed ($F_n > 1$) of the ACV, the transmission force coefficient generally accounts for a very low proportion of the wave force. That is, excitation from the transmission component can be considered negligible while sailing at cruising speed.

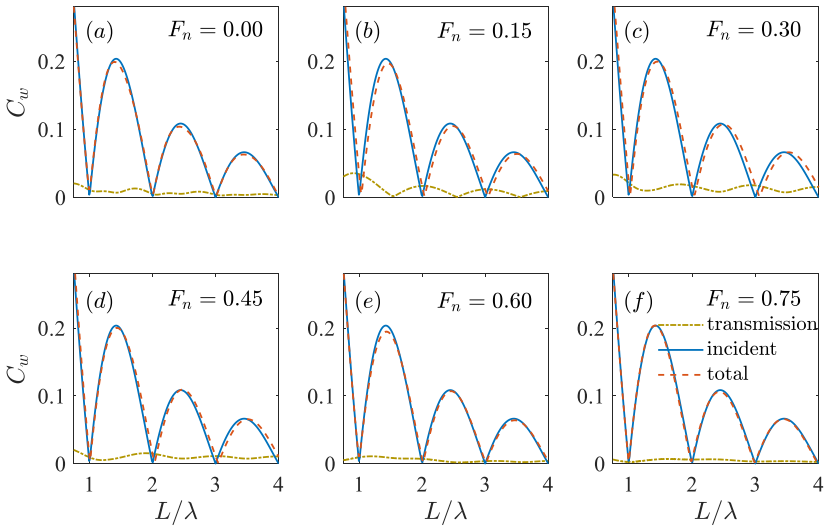

Fig. 19. Wave force coefficients as a function of incident wavelength (d/L = 3.58, $\tilde{p}_0 = \frac{\text{0.0127}}{\text{0.0100}}$).

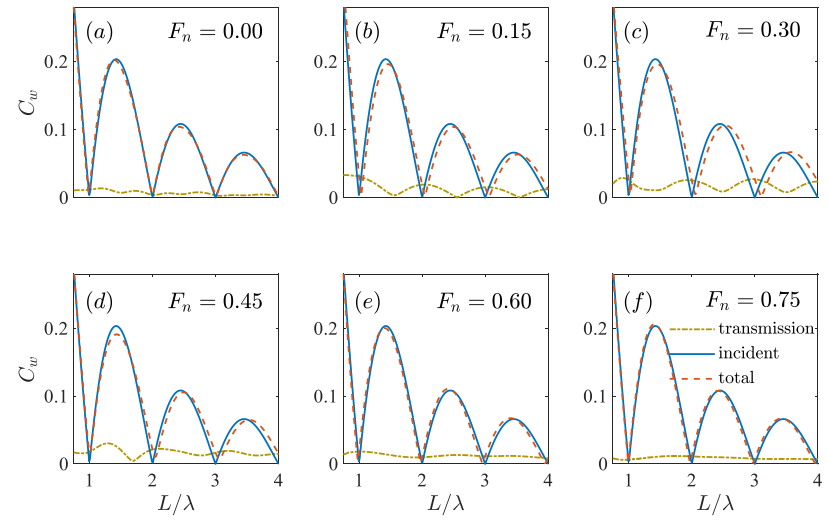

Fig. 20. Wave force coefficients as a function of incident wavelength (d/L = 0.215, $\tilde{p}_0 = \frac{\text{0.0127}}{\text{0.0100}}$).

Wave force is not the only element responsible for the motion of the hovercraft in waves, as wave elevation below the hull also plays a role. In the cushion system, a gap between the

skirt and the water surface allows the air to leak out, and this distance is called the leakage height. In a regular wave, the leakage height varies periodically, and the air cushion system is no longer steady, resulting in heave and pitch motions (Reynolds *et al*., 1972). In addition to the incident wave system, the transmission wave system may also affect wave elevation. Fig. 21 illustrates the amplitude of the transmission patterns, where A is the amplitude of the incident wave, and $\tilde{p}_0$ is the dimensionless pressure. The wave elevation of the transmission component is mainly reflected on the aft side of the hull and the wake. The effects of the transmission component in shallow water are slightly more significant than those in deep water. Several similarities between the transmission waves and the ACV wakes can be seen in Fig. 21: the transmission waves consist of divergent and transverse waves and are contained within a certain angle following the ACV. The dimensionless factor $\tilde{p}_0$ is typically in the range of 0.01–0.02, so the height of the transmission waves may reach 7–20% of the incident wave height. We hope that this part of the work may serve as a reference for future work on the motion response of the ACV in waves.

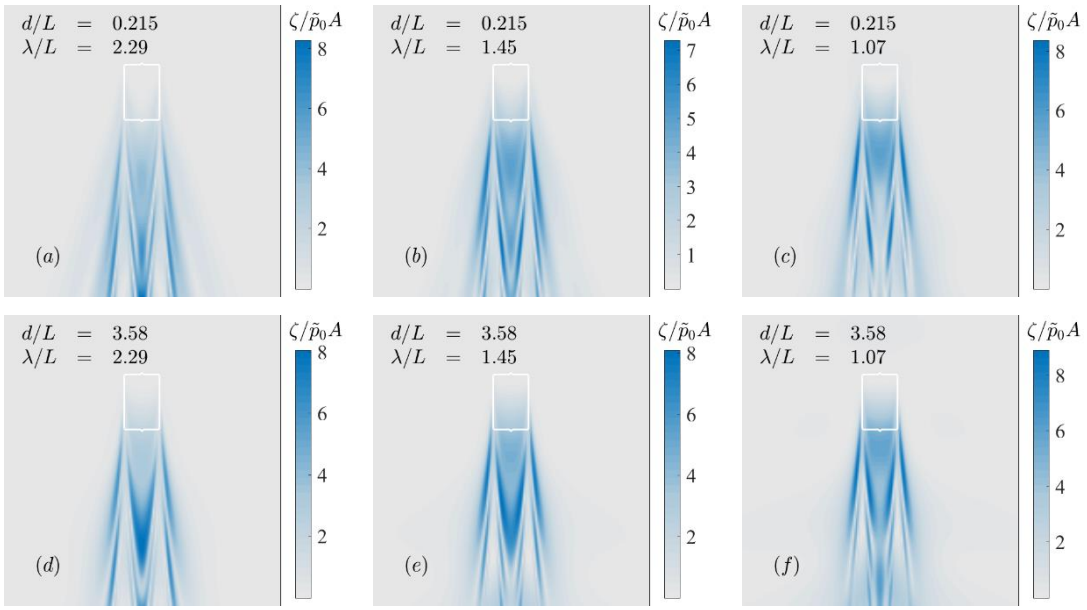

Fig. 21. Transmission wave amplitude patterns in different incident wave length (a)–(c) d/L = 0.215, $\tilde{p}_0 = 0.0127$, F_n = 1.5 (d)–(f) d/L = 3.58, $\tilde{p}_0 = 0.0127$, F_n = 1.5.

4. Conclusions

This paper set out to investigate the nonlinear effects of cushion pressures on the ACV wake system. In the study, we simplified the ACV into a predefined pressure distribution, without taking splash and skirt-water contact into account. For the nonlinear wake of the pressure distribution, we extended the HOS method in an earth-fixed coordinate system to perform time-domain simulations. An attention mechanism was applied to reconstruct the computational domain and absorb far-field disturbance waves so that the ACV would remain

at the center of the domain. These techniques considerably reduce the computation effort. When we perform the calculations on the GPU, it takes only 0.02s per timestep with a 512 × 512 grid. For verification, we also derived the perturbation solutions of ACV wakes in a moving reference system, see Appendix.

The nonlinear method was subsequently used to investigate the nonlinear waves generated by an ACV. For a constant-speed ACV in calm water, the low-pressure results predicted by the nonlinear method are in perfect agreement with the linearized solution, while the high-pressure results show more nonlinear features. Simulations suggest that the nonlinearity is more pronounced in shallow water and low-speed cases. If the nonlinear effects of cushion pressure are considered, the wake system exhibits shorter wavelengths, steeper wave crests, and flatter wave troughs than the linear predictions. The nonlinear effects on wave drag are not as significant as those of wave elevation. Wave resistance in deep water is virtually unaffected by nonlinearity. In shallow water, nonlinearity causes the resistance hump to become broader and lower in the resistance-velocity curve. Similar findings were also described by Bhushan *et al*. (2011).

For accelerating motion, the time-domain approach in the paper is shown to yield results consistent with the linear predictions proposed by previous researchers (Doctors and Sharma, 1972; Yeung, 1975). The presence of acceleration shifts the resistance hump and hollow towards higher Froude numbers and significantly decreases the peak resistance in shallow water. As an extension to the published literature, this paper also investigates the nonlinear effect in the acceleration motion. Numerical simulations demonstrate that wave nonlinearity barely affects the deep-water acceleration resistance. In shallow water, contrary to the significant resistance drop observed in constant-speed cases, the nonlinear resistance curve does not differ much from the linear predictions for acceleration motion. This could be explained by the fact that the acceleration process does not take enough time to generate the solitary wave in front of the bow. In shallow water, the nonlinearity shifts the resistance hump slightly to the left during acceleration, and the greater the acceleration, the weaker the nonlinear effect.

For the ACV in waves, we have identified and studied the nonlinear transmission components resulting from interactions between the incident wave system and the ACV wake system. The nonlinear time-domain simulations were compared to our derived frequency-domain perturbation solutions. The results obtained by the two methods are in good agreement, which validates the time-domain approach and suggests that a major component of the transmission components is of second order. For a cruising ACV, the presence of this wave component does not strongly affect the wave force but contributes to periodic variation in wave elevation on the aft side of the ACV, eventually influencing the motion response.

The nonlinear effects on the accelerating motion and the transmission components are here investigated for the first time. We hope that the findings may provide guidance for the resistance and sea-keeping performance of ACVs. An air cushion system is a complex system impacted by the fan, skirt, wave surface below, air compressibility, and other features. The pressure pulsates during navigation, particularly in regular waves. However, the ACV in this paper is idealized as a time-constant pressure distribution. In the future, the time-varying model of cushion pressure distribution with fans and air leakage considered may be added to the proposed method, so that the coupling effects of pressure distribution, motion response, and wake pattern can be considered, eventually obtaining more realistic results.

Appendix. Perturbation derivation

A.1 Basic equations

Consider a pressure distribution moving along the *x*-axis at speed *U*, boundary conditions under the moving reference frame are written as:

$$\zeta_t + \nabla_x\phi\cdot\nabla_x\zeta - U\zeta_x - \phi_z = 0 \quad on \quad z=\zeta \tag{1}$$

$$\phi_t - U\phi_x + g\zeta + \frac{1}{2}(\nabla\phi)^2 + \frac{p}{\rho} = 0 \quad on \quad z=\zeta \tag{2}$$

where p represents the pressure distribution of an ACV. By operating material derivative D/Dt on Eq. (1), we obtain:

$$\begin{aligned} & \phi_{tt} - 2U\phi_{xt} + U^2\phi_{xx} + 2\nabla\phi\cdot\nabla\phi_t - 2\nabla\phi\cdot\nabla\phi_x \\ + \;& g\phi_z + \frac{1}{2}\nabla\phi\cdot\nabla(\nabla\phi\cdot\nabla\phi) \qquad\qquad on \quad z=\zeta \\ + \;& \frac{1}{\rho}(-Up_x + \nabla_x\phi\cdot\nabla_x p) \\ = \;& 0 \end{aligned} \tag{3}$$

In order to identify the effects of the pressure term and the incident wave, the formal expressions are substituted to Eq. (1) and Eq. (3):

$$\begin{aligned} \zeta &= \alpha\zeta^{10} + \beta\zeta^{01} + \alpha\beta\zeta^{11} + \beta^2\zeta^{02} + \alpha\beta^2\zeta^{12} + \dots \\ \phi &= \alpha\phi^{10} + \beta\phi^{01} + \alpha\beta\phi^{11} + \beta^2\phi^{02} + \alpha\beta^2\phi^{12} + \cdots \\ p &= \alpha p^{10} \end{aligned} \tag{4}$$

where terms with α indicate the contribution of the pressure term, terms with β indicate the contribution of the incident wave. Here β is the independent small quantity proportional to the surface slopes.

Now expand Eq. (1) and Eq. (3) in Taylor series about z=0, and combine the terms with coefficients of $\alpha\beta^j$. The terms in α, β give the following equations respectively

$$\begin{cases} g\zeta^{01} + \phi_t^{01} - U\phi_x^{01} = 0 & on \;\; z = 0 \\ \phi_{tt}^{01} + g\phi_z^{01} - 2U\phi_{xt}^{01} + U^2\phi_{xx}^{01} = 0 & on \;\; z = 0 \end{cases} \tag{5}$$

$$\begin{cases} g\zeta^{10} + \phi_t^{10} - U\phi_x^{10} + \dfrac{p^{10}}{\rho} = 0 & on \;\; z = 0 \\ \phi_{tt}^{10} + g\phi_z^{10} - 2U\phi_{xt}^{10} + U^2\phi_{xx}^{10} - \dfrac{U}{\rho}p_x^{10} = 0 & on \;\; z = 0 \end{cases} \tag{6}$$

and terms in $\alpha\beta$ gives

$$\begin{cases} g\zeta^{11} + \phi_t^{11} - U\phi_x^{11} + F_1 = 0 & on \;\; z = 0 \\ \phi_{tt}^{11} + g\phi_z^{11} - 2U\phi_{xt}^{11} + U^2\phi_{xx}^{11} + F_2 = 0 & on \;\; z = 0 \end{cases} \tag{7}$$

where

$$\begin{aligned} F_1 &= \nabla\phi^{01}\cdot\nabla\phi^{10} + \zeta^{10}(\phi_{zt}^{01} - U\phi_{xz}^{01}) + \zeta_{01}(\phi_{zt}^{10} - U\phi_{xz}^{10}) \\ F_2 &= 2\nabla\phi^{10}\cdot\nabla(\phi_t^{01} - U\phi_x^{01}) + 2\nabla\phi^{01}\cdot\nabla(\phi_t^{10} - U\phi_x^{10}) \\ &+ \zeta^{10}(\phi_{ztt}^{01} + g\phi_{zz}^{01} - 2U\phi_{xzt}^{01} + U^2\phi_{xxz}^{01}) \\ &+ \zeta^{01}(\phi_{ztt}^{10} + g\phi_{zz}^{10} - 2U\phi_{xzt}^{10} + U^2\phi_{xxz}^{10}) \\ &+ \frac{1}{\rho}(\nabla_x\phi^{01}\cdot\nabla_x p^{10}) \end{aligned} \tag{8}$$

A.2 Solutions of the first order equation

Eq. (5) basically describes the Airy wave in a moving reference system, whose general solution is

$$\phi^{01} = -\frac{igA}{\omega + k_x U}\frac{\cosh(kz + kd)}{\cosh(kd)}e^{ik_x x + ik_y y - i\omega t} \tag{9}$$

where

$$\begin{aligned} \omega &= \sqrt{gk\tanh(kd)} - k_x U \\ k &= \sqrt{k_x^2 + k_y^2} \end{aligned} \tag{10}$$

When the motion is steady, time derivative terms in Eq. (6) can be eliminated. The combined free-surface condition could be modified to

$$g\phi_z^{10} + U^2\phi_{xx}^{10} - \mu U\phi_x^{10} = \frac{U}{\rho}p_x^{10} \qquad on \;\; z = 0 \tag{11}$$

The form of Eq. (11) is exactly the same as that given by Doctors (1993) , which represents

the linearized steady flow field. Here an artificial viscosity term μ is introduced to help control the dissipation of far-field waves (DePrima and Wu, 1957). The solution can be derived by a double Fourier transform as below

$$\phi^{10} = \frac{1}{4\pi^2}\iint \frac{\iint \frac{U}{\rho}\frac{\partial p}{\partial x} e^{-i(kx+ly)}dxdy}{\omega_{kl}^2 - U^2k^2 - i\mu kU} e^{i(kx+ly)}dkdl \tag{12}$$

where

$$\omega_{kl}^2 = g\sqrt{k^2+l^2}\tanh\sqrt{k^2+l^2}d \tag{13}$$

A.3 Solutions of the second order equation

ϕ^{11} gives a second-order approximation of the interaction between the steadily-moving ACV and the incident wave. When the incident wave is regular, the potential function ϕ^{11} varies periodically. We transform Eq. (7) into the frequency domain with artificial viscosity terms

$$-\omega^2\phi^{11} + g\phi_z^{11} + 2i\omega U\phi_x^{11} + U^2\phi_{xx}^{11} - i\omega\mu\phi^{11} - \mu U\phi_x + F_2 = 0 \quad on \;\; z = 0 \tag{14}$$

where

$$\begin{aligned} F_2 &= 2\nabla\phi^{10}\cdot\nabla(-i\omega\phi^{01} - U\phi_x^{01}) - 2U\nabla\phi^{01}\cdot\nabla\phi_x^{10} \\ &+ \zeta^{10}(-\omega^2\phi_z^{01} + g\phi_{zz}^{01} + 2i\omega U\phi_{xz}^{01} + U^2\phi_{xxz}^{01}) \\ &+ \zeta^{01}(g\phi_{zz}^{10} + U^2\phi_{xxz}^{10}) \\ &+ \frac{1}{\rho}(\nabla_x\phi^{01}\cdot\nabla_x p^{10}) \end{aligned} \tag{15}$$

Finally, the solution of the second-order interaction term could be derived by a double Fourier transform

$$\phi_{11} = \frac{1}{4\pi^2}\iint \frac{\iint -F_2(x,y,t)e^{-i(kx+ly)}dxdy}{\omega_{kl}^2 - (\omega+Uk)^2 - i\mu(\omega+Uk)} e^{i(kx+ly)}dkdl \tag{16}$$

Reference

Barratt, M.J., 1965. The wave drag of a hovercraft. J. Fluid Mech. 22(1), 39-47.

Bhushan, S., Stern, F., Doctors, L.J., 2011. Verification and Validation of URANS Wave Resistance for Air Cushion Vehicles, and Comparison With Linear Theory. J. Ship Res., 55(4), 249–267.

Bhushan, S., Mousaviraad, M., Stern, F., 2017. Assessment of URANS surface effect ship models for calm water and head waves. Appl. Ocean Res. 67, 248-262.

Boussinesq, J., 1872. Théorie des ondes et des remous qui se propagent le long d'un canal rectangulaire horizontal, en communiquant au liquide contenu dans ce canal des vitesses sensiblement pareilles de la surface au fond. Journal de mathématiques pures et appliquées, 55-108.

Clamond, D., Grue, J., 2001. A fast method for fully nonlinear water-wave computations. J. Fluid Mech. 447, 337-355.

Clamond, D., Fructus, D., Grue, J., Kristiansen, Ø., 2005. An efficient model for three-dimensional surface wave simulations. Part II: Generation and absorption. J. Comput. Phys. 205(2), 686-705.

Colen, J., Kolomeisky, E. B., 2021. Kelvin–Froude wake patterns of a traveling pressure disturbance. Eur. J. Mech. B Fluids 85, 400-412.

Dam, K.T., Tanimoto, K., Nguyen, B.T., Akagawa, Y., 2006. Numerical study of propagation of ship waves on a sloping coast. Ocean Eng. 33(3-4), 350-364.

Dam, K.T., Tanimoto, K., Fatimah, E., 2008. Investigation of ship waves in a narrow channel. Journal of marine science and technology, 13(3), 223-230.

David, C.G., Roeber, V., Goseberg, N., Schlurmann, T., 2017. Generation and propagation of ship-borne waves-Solutions from a Boussinesq-type model. Coast. Eng. 127, 170-187.

De Prima, C.R., Wu, T.Y.T., 1957. On the theory of surface waves in water generated by moving disturbances. Calif. Inst. Tech. Eng. Div. Rep. 21–23.

Doctors, L.J., Sharma, S.D., 1972. The wave resistance of an air-cushion vehicle in steady and accelerated motion. J. Ship Res. 16(04), 248-260.

Doctors, L.J., 1975. The experimental wave resistance of an accelerating two-dimensional pressure distribution. J. Fluid Mech. 72(3), 513-527.

Doctors, L.J., Dagan, G., 1980. Comparison of nonlinear wave-resistance theories for a two-dimensional pressure distribution. J. Fluid Mech. 98(3), 647-672.

Doctors, L.J., 1993. On the Use of Pressure Distributions to Model the Hydrodynamics of Air-Cushion Vehicles and Surface- Effect Ships. Naval engineers journal 105(2), 69-89.

Dommermuth, D.G., Yue, D.K., 1987. A high-order spectral method for the study of nonlinear gravity waves. J. Fluid Mech. 184, 267-288.

Dommermuth, D.G., Yue, D.K., 1988. The nonlinear three-dimensional waves generated by a moving surface disturbance. In Proceedings of 17th Symposium on Naval Hydrodynamics, Hague, Netherlands.

Everest, J.T., 1966. Shallow water wave drag of rectangular hovercraft. National Physical Laboratory, NPL, Ship Division, Ship Report 79.

Everest. J.T., Hogben, N., 1967. Research on hovercraft over calm water. Trans, Royal Institution of Naval Architects. 111, 3, 343-365

Fructus, D., Clamond, D., Grue, J., Kristiansen, Ø., 2005. An efficient model for three-dimensional surface wave simulations: Part I: Free space problems. J. Comput. Phys. 205(2), 665-685.

Fructus, D., Grue, J., 2007. An explicit method for the nonlinear interaction between water waves and variable and moving bottom topography. J. Comput. Phys. 222(2), 720-739.

Fuhrman, D.R., Bingham, H.B., Madsen, P.A., Thomsen, P.G., 2004. Linear and non-linear stability analysis for finite difference discretizations of high order Boussinesq Eq.s. Int. J. Numer. Meth. Fl. 45(7), 751-773.

Gao, X., Xu, S., Tang, W., 2021. Hybrid analytic-FEM approach for dynamic response analysis of air-cushion vehicle skirts. Mar. Struct. 79, 103062.

Grue, J., 2017. Ship generated mini-tsunamis. J. Fluid Mech. 816, 142-166.

Guo, Z., Ma, Q.W., Qin, H., 2018. A novel 2.5 D method for solving the mixed boundary value problem of a surface effect ship. Appl. Ocean Res. 78, 25-32.

Havelock, T.H., 1914. Ship resistance: The wave-making properties of certain travelling pressure disturbances. In: Proceedings of the Royal Society of London. Series A, Containing Papers of a Mathematical and Physical Character 89(613), 489-499.

Havelock, T.H., 1932. The theory of wave resistance. In: Proceedings of the Royal Society of London. Series A, Containing Papers of a Mathematical and Physical Character 138(835), 339-348.

Jamois, E., Fuhrman, D.R., Bingham, H.B., Molin, B., 2006. A numerical study of nonlinear wave run-up on a vertical plate. Coast. Eng. 53(11), 929-945.

Kerczek, V.C., Salvesen, N., 1977. Nonlinear free-surface effects--the dependence on Froude Number. In: Proceedings of the Second International Conference on Numerical Ship Hydrodynamics, University of California, Berkeley.

Li, Y., Sclavounos, P. D., 2002. Three-dimensional nonlinear solitary waves in shallow water generated by an advancing disturbance. J. Fluid Mech. 470, 383-410.

Li, Y., Liu, J., Hu, M., Zhang, Z., 2017. Numerical modeling of ice-water system response based on Rankine source method and finite difference method. Ocean Eng. 138, 1-8.

Lord Kelvin (William Thomson), 1887. On ship waves. In: Proceedings of the Royal Society of Edinburgh 38, 409–434.

Lunde, J.K., 1951. On the linearized theory of wave resistance for displacement ships in steady and accelerated motion. Trans soc naval archit mar eng 59, 25-76.

Madsen, P.A., Bingham, H.B., Liu, H., 2002. A new Boussinesq method for fully nonlinear waves from shallow to deep water. J. Fluid Mech. 462, 1-30.

Maki, K.J., Broglia, R., Doctors, L.J., Di Mascio, A., 2012. Nonlinear wave resistance of a two-dimensional pressure patch moving on a free surface. Ocean Eng., 39, 62-71.

Maki, K.J., Broglia, R., Doctors, L.J., Di Mascio, A., 2013. Numerical investigation of the components of calm-water resistance of a surface-effect ship. Ocean Eng., 72, 375-385.

Newman, J.N., Poole, F.A.P., 1962. The wave resistance of a moving pressure distribution in a canal. Schiffstechnik 9, 21–26.

Nikseresht, A.H., Alishahi, M.M., Emdad, H., 2008. Complete flow field computation around an ACV (air-cushion vehicle) using 3D VOF with Lagrangian propagation in computational domain. Comput. Struct. 86(7-8), 627-641.

Noblesse, F., Delhommeau, G., Yang, C., 2009. Practical evaluation of steady flow resulting from a free-surface pressure patch. J. Ship Res. 53 (3), 137–150.

Noblesse, F., Delhommeau, G., Huang, F., Yang, C., 2011. Practical mathematical representation of the flow due to a distribution of sources on a steadily advancing ship hull. J. Eng. Math. 71(4), 367-392.

Pethiyagoda, R., McCue, S.W., Moroney, T.J., 2017. Spectrograms of ship wakes: identifying linear and nonlinear wave signals. J. Fluid Mech. 811, 189-209.

Pethiyagoda, R., Moroney, T.J., Macfarlane, G.J., Binns, J.R., McCue, S.W., 2018. Time-frequency analysis of ship wave patterns in shallow water: modelling and experiments. Ocean Eng. 158, 123-131.

Pethiyagoda, R., Moroney, T.J., Lustri, C.J., McCue, S.W., 2021. Kelvin wake pattern at small Froude numbers. J. Fluid Mech. 915.

Reynolds, A.J., West, R.P., Brooks, B.E., 1972. Heaving and pitching response of a hovercraft moving over regular waves. J. Mech. Eng. Sci. 14(5), 340-352.

Schwartz, L.W., 1981. Nonlinear solution for an applied overpressure on a moving stream. J. Eng. Math. 15(2), 147-156.

Shi, F., Malej, M., Smith, J.M., Kirby, J.T., 2018. Breaking of ship bores in a Boussinesq-type ship-wake model. Coast. Eng. 132, 1-12.

Sturova, I.V., Tkacheva, L.A., 2019. Moving Pressure Distribution in an Ice Channel. In 34th International Workshop on Water Waves and Floating Bodies, 7-10.

Sung, H.G., Grilli, S.T., 2008. BEM computations of 3-d fully nonlinear free-surface flows caused by advancing surface disturbances. International Journal of Offshore and Polar Engineering, 18(04).

Torsvik, T., Soomere, T., 2008. Simulation of patterns of wakes from high-speed ferries in Tallinn Bay. Estonian Journal of Engineering, 14(3), 232-254.

Torsvik, T., Soomere, T., Didenkulova, I., Sheremet, A., 2015. Identification of ship wake structures by a time–frequency method. J. Fluid Mech. 765, 229-251.

West, B.J., Brueckner, K.A., Janda, R.S., Milder, D.M., Milton, R.L., 1987. A new numerical method for surface hydrodynamics. J. Geophys. Res. Oceans 92(C11), 11803-11824.

Xiao, Q., Zhu, R., Huang, S., 2019. Hybrid time-domain model for ship motions in nonlinear extreme waves using HOS method. Ocean Eng. 192, 106554.

Xiao, W., Liu, Y., Wu, G., Yue, D.K., 2013. Rogue wave occurrence and dynamics by direct simulations of nonlinear wave-field evolution. J. Fluid Mech. 720, 357-392.

Xue, Y.Z., Zeng, L.D., Ni, B.Y., Korobkin, A.A., Khabakhpasheva, T.I., 2021. Hydroelastic response of an ice sheet with a lead to a moving load. Phys. Fluids 33(3), 037109.

Yeung, R.W., 1975. Surface waves due to a maneuvering air-cushion vehicle. J. Ship Res. 19(04), 224-242.

Zakharov, V.E., 1968. Stability of periodic waves of finite amplitude on the surface of a deep fluid. J. Appl. Mech. Tech. Phys. 9(2), 190-194.